JGR Solid Earth

RESEARCH ARTICLE
10.1029/2022JB025425

Three-Dimensional Basin Depth Map of the Northern Los Angeles Basins From Gravity and Seismic Measurements

Valeria Villa[1], Yida Li[1], Robert W. Clayton[1], and Patricia Persaud[2,3]

[1]California Institute of Technology, Pasadena, CA, USA, [2]Louisiana State University, Baton Rouge, LA, USA, [3]University of Arizona, Tucson, AZ, USA

Key Points:

- Passive seismic and gravity measurements are integrated to estimate the 3D depth of the northern Los Angeles basins
- The maximum depth in the San Gabriel basin is ~4.5 km, and Chino and San Bernardino basins are less than 2 km deep
- The use of gravity helps to delineate faults across the basin, which helps our sediment-basement interpretation in the receiver functions

Supporting Information:

Supporting Information may be found in the online version of this article.

Correspondence to:

V. Villa,
vvilla@caltech.edu

Citation:

Villa, V., Li, Y., Clayton, R. W., & Persaud, P. (2023). Three-dimensional basin depth map of the northern Los Angeles basins from gravity and seismic measurements. *Journal of Geophysical Research: Solid Earth*, *128*, e2022JB025425. https://doi.org/10.1029/2022JB025425

Received 19 AUG 2022
Accepted 11 JUL 2023

Author Contributions:

Conceptualization: Valeria Villa, Robert W. Clayton
Data curation: Valeria Villa, Yida Li, Robert W. Clayton, Patricia Persaud
Formal analysis: Valeria Villa, Yida Li
Funding acquisition: Robert W. Clayton, Patricia Persaud
Investigation: Valeria Villa, Yida Li, Robert W. Clayton, Patricia Persaud
Methodology: Valeria Villa, Yida Li, Robert W. Clayton
Project Administration: Robert W. Clayton, Patricia Persaud
Resources: Robert W. Clayton, Patricia Persaud
Software: Valeria Villa
Supervision: Robert W. Clayton
Validation: Valeria Villa, Yida Li, Robert W. Clayton, Patricia Persaud

Abstract The San Gabriel, Chino, and San Bernardino sedimentary basins in Southern California amplify earthquake ground motions and prolong the duration of shaking due to the basins' shape and low seismic velocities. In the event of a major earthquake rupture along the southern segment of the San Andreas fault, their connection and physical proximity to Los Angeles (LA) can produce a waveguide effect and amplify strong ground motions. Improved estimates of the shape and depth of the sediment-basement interface are needed for more accurate ground-shaking models. We obtain a three-dimensional basement map of the basins by integrating gravity and seismic measurements. The travel time of the sediment-basement *P*-to-*S* conversion, and the Bouguer gravity along 10 seismic lines, are combined to produce a linear relationship that is used to extend the 2D profiles to a 3D basin map. Basement depth is calculated using the predicted travel time constrained by gravity with an *S*-wave velocity model of the area. The model is further constrained by the basement depths from 17 boreholes. The basement map shows the south-central part of the San Gabriel basin is the deepest part and a significant gravity signature is associated with our interpretation of the Raymond fault. The Chino basin deepens toward the south and shallows northeastward. The San Bernardino basin deepens eastward along the edge of the San Jacinto Fault Zone. In addition, we demonstrate the benefit of using gravity data to aid in the interpretation of the sediment-basement interface in receiver functions.

Plain Language Summary The shaking levels in the Los Angeles (LA) metropolitan area due to an earthquake on the San Andreas fault are underestimated. Northeast of LA, the San Gabriel, Chino, and San Bernardino basins influence the amount of shaking the LA area will experience. Sedimentary basins like these can amplify and trap seismic waves. Understanding these basins' shapes will improve our Earth model of the area and therefore seismic hazard estimates. The Basin Amplification Seismic Investigation project installed several small seismic instruments across these basins to characterize the structure of the basins. Along with gravity measurements, which capture information about the rock's density variations, we determine the basins' depth and shape. The depth model is then combined with a new velocity model of the area to produce an improved Earth model. Future studies of ground shaking should take these improved models into account.

1. Introduction

In the event of a large earthquake rupture, sedimentary basins in the greater Los Angeles (LA) area pose a significant seismic hazard. The Los Angeles Basin (LAB) is situated underneath the mega-city of LA, a metropolitan city with a growing population. Extensive oil and gas exploration in the area provided a rich data set of the subsurface for detailed basin mapping purposes. Northeast of the LAB is the San Gabriel, Chino, and San Bernardino basins (Figure 1a). The shape and depth of these basins are not well constrained because of the lack of seismic surveys in the area, particularly active source surveys used for oil and gas exploration. During a large earthquake rupture, the basins trap and amplify seismic waves which highly depend on the thickness, geometry, and material properties of the sedimentary layers within the basin (Frankel, 1993). A wave-guide effect between these northern basins and the LAB is hypothesized. The hypothesized waveguide effect channels the amplified energy toward downtown LA for events on the southern San Andreas fault (Olsen et al., 2006). Current ground-shaking models for the greater LA area appear to underestimate the level of ground shaking for earthquakes on the southern segment of the San Andreas fault by a factor of 4 (Denolle et al., 2014). Accurate knowledge of the basins' shape and edges will help resolve localized amplification and interference effects (Magistrale et al., 2000) and help to give insight into the pattern of ground shaking the local population may experience.

Visualization: Valeria Villa, Yida Li
Writing – original draft: Valeria Villa

The primary goal of the Basin Amplification Seismic INvestigation (BASIN) project is to improve the 3D seismic velocity model and structural knowledge of the basins in the northern LA area. This improved model will help to provide a better estimate of ground shaking. Here, we integrate results from the BASIN receiver function (RF) profiles (Ghose et al., 2023; Liu et al., 2018; Wang et al., 2021) with gravity data and use a 3D seismic velocity (V_s) model obtained from the BASIN data set (Li et al., 2023) to map the basement depth of the San Gabriel, Chino, and San Bernardino basins. Previous geophysical studies, borehole data, groundwater management reports, and geologic maps are used as additional constraints on the final model. The advantage of this approach is that it allows us to extend the detailed sediment-basement depths from our dense nodal survey to produce the first integrated basin model for the region.

1.1. Geologic Setting

The San Gabriel basin is a triangular-shaped sedimentary basin bounded by the San Gabriel Mountains on the north, San Jose and Puente Hills on the east, and Repetto and Montebello Hills on the west (Yeats, 2004; Figure 1). The Pliocene-Pleistocene sedimentary fill is comprised of a basal shallow-marine sequence overlain by the non-marine Duarte Conglomerate and underlain by a basement boundary composed of the Peninsular Ranges batholithic and metamorphic rocks such as gneiss (Brocher, 2005; Fuis et al., 2001; Yeats, 2004). Major faults bound the sedimentary fill of the basin with the Sierra Madre fault on the north and Puente Hills blind-thrust in the south (Figure 1b). The west side is marked by the northwest-striking, right-slip East-Montebello fault; and the east side by the northeast-striking, left-slip Walnut Creek fault and Indian Hill fault (Figure 1b). The northeast-striking segment of the Raymond fault separates the deeper San Gabriel basin from the shallower Raymond basin. Weaver and Dolan (2000) reported a 3.4 km left-lateral offset of a crystalline basement ridge at the east end of the Raymond fault. Wright (1991), Brocher (2005), and Fuis et al. (2001) estimated the maximum depth of the San Gabriel basin as 3, 3.7, and 5 km, respectively. Yeats (2004) inferred the basin trends with a southwest depression toward the Montebello and Repetto Hills and an upward plunge toward the Raymond fault.

The Chino basin is one of the largest groundwater basins in Southern California and the largest in the upper Santa Ana Valley. It is bounded by the Puente Hills on the west, the Jurupa Hills on the southeast, and the San Gabriel Mountains on the north (Figure 1a). The basin is fault bounded by the northeast-striking San Jose fault, northeast-striking Cucamonga fault, southeast-striking Chino fault, and northwest-striking Rialto-Colton fault (Figure 1b). Tectonic forces uplifted neighboring mountains and depressed the basin along major fault zones (Wildermuth et al., 2005). The depth of groundwater in the northernmost and southernmost parts is less than 152 and 4.50 m, respectively, and groundwater movement is from north to south (Blomquist, 2021; Dutcher & Garrett, 1963). The bedrock is comprised of a mix of metamorphic, igneous, and consolidated sedimentary rocks.

The San Bernardino basin is a wedge-shaped sedimentary basin bounded by two major fault zones: the San Jacinto Fault zone (SJFZ) to the west and the San Andreas Fault zone (SAFZ) to the east (Figure 1b). The San Gabriel and San Bernardino Mountains border the northern and eastern sides of the basin. The basin's deepest part resembles a pull-apart structure from the Quaternary extension of the major right-step faults of the San Jacinto and SAFZs (Anderson et al., 2004; Morton & Miller, 2006). The filling of unconsolidated Quaternary and Tertiary alluvial-fan deposits covers the consolidated, non-water-bearing Tertiary deposits (Dutcher & Garrett, 1963; Frankel, 1993). The sedimentary section overlies the pre-Tertiary igneous and metamorphic basement rocks (Dutcher & Garrett, 1963). The basement rock types are composed of Peninsular Ranges-type (i.e., granodiorite, quartz diorite, tonalite, and gabbro), San Gabriel Mountains-type (Pelona Schist, and prebatholic crystalline rocks intruded by Mesozoic plutons), Southeastern San Gabriel Complex (i.e., granitic rocks, migmatite, and gneiss), and San Bernardino Mountain-type (Anderson et al., 2004).

There are a few basement depths documented in the San Bernardino basin from water and oil wells, and records mostly cover the northeastern edges of the basin with a maximum basement depth of around 1.2 km (Dutcher & Garrett, 1963). Stephenson (2002) studied 14 km of seismic reflection data through the San Bernardino area and inferred a depth of 1.7 km near the San Jacinto fault. Anderson et al. (2004) combined gravity and aeromagnetic data to map the San Bernardino basin and found that the largest amount of extension is along the San Jacinto fault with a maximum depth of 2 km. Catchings et al. (2008) found a shallower basin depth (closer to 1.2 km) based on two seismic profiles in the San Bernardino basin.

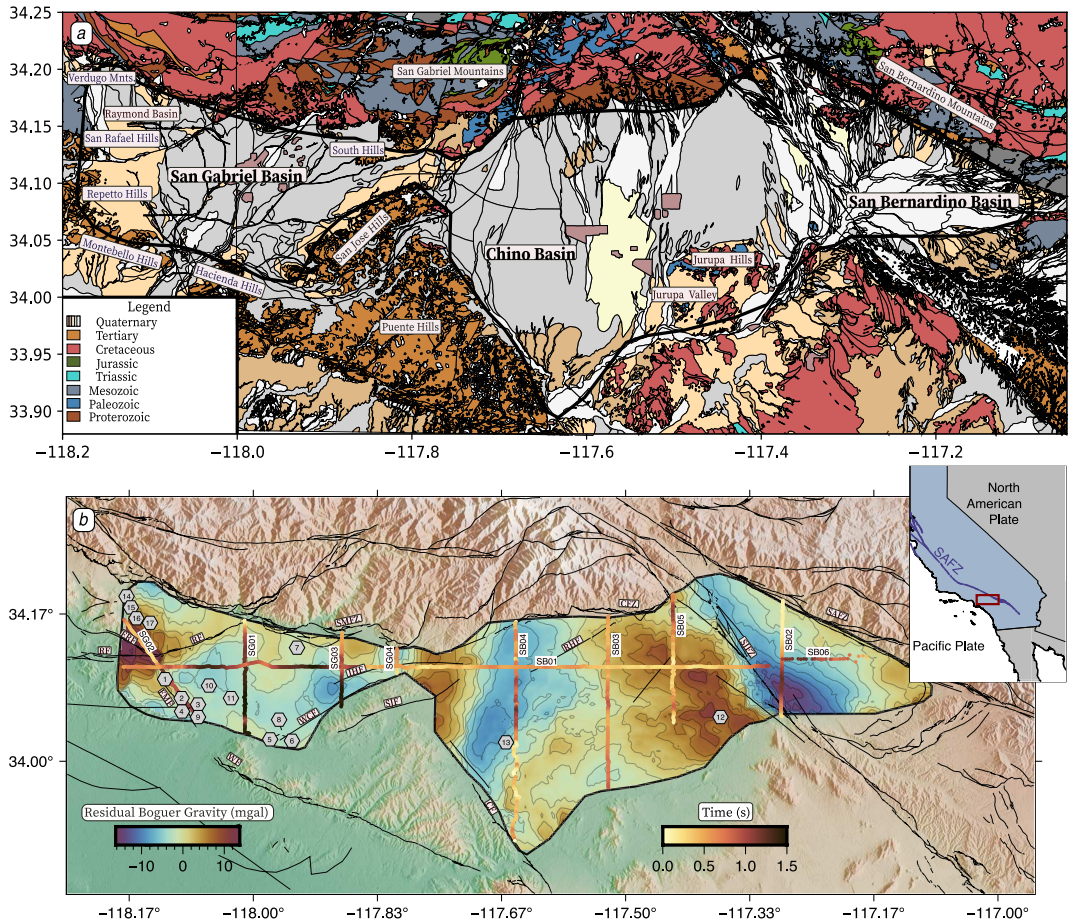

Figure 1. (a) Geologic map of the northern Los Angeles basins adapted from Yerkes and Campbell (2005) and Morton and Miller (2006). The geologic age of the units is shown in the legend. (b) Shaded-relief terrain map showing the outline of the Basin Amplification Seismic Investigation survey. The contoured grid depicts the residual Bouguer gravity. Dark red-yellow-white circles show the time-to-basement in seconds along the 10-node lines. Black thin lines are fault locations (Jennings & Bryant, 2010). Numbered symbols mark the locations of the boreholes used in this study. Table 1 shows the fault names and abbreviations. The inset map depicts the regional context of the study area at the transform plate boundary between the Pacific and North American plates.

2. Data and Methods

2.1. BASIN Project and Receiver Functions

This study integrates seismic and gravity measurements to determine the shape and depth of the San Gabriel, Chino, and San Bernardino basins. The BASIN project deployed approximately 744 seismic nodes from 2017 to 2019, across 10 lines with an average 250-m spacing (Figure 1). The dense intra-line spacing provides the spatial detail used to constrain the basement shape. The prefix SG is used for lines in the San Gabriel basin and SB for lines in the Chino or San Bernardino basin. Seismic line SB1 crosses all three northern basins and is the longest line. The San Gabriel basin has four lines: SG2, SG1, SG3, and SG4; the Chino basin has three lines: SB4, SB3, and SB5; and the San Bernardino basin has two lines: SB2, SB6, with the basins and lines listed from west to east.

RFs were computed along the 10 seismic lines by three principal studies within the BASIN project (Ghose et al., 2023; Liu et al., 2018; Wang et al., 2021). These studies concentrated on acquiring the basement-sediment interface, other intra-crustal layers, and the Moho discontinuity, as well as characterizing possible fault offsets. Travel times associated with the sediment-basement interface were determined from the *P*-to-*S* converted phases in the RFs. Liu et al. (2018) applied traditional frequency domain deconvolution to teleseismic events from a 35-day nodal data set along SG1, SG2, and SB4 and showed the Moho discontinuity, basement bottom, intermediary sedimentary layers, and offsets associated with the Red Hill and Raymond faults. Wang et al. (2021) used a

Table 1
Fault Abbreviations Used in Figures 1b and 7a and Their Full Names

Abbreviation = IHF	Fault name = Indian Hill Fault
CF	Chino Hill Fault
CFZ	Cucamonga Fault Zone
EMF	East Montebello Fault
ERF	Eagle Rock Fault
RF	Raymond Fault
RHF	Red Hill Fault
RCF	Rialto-Colton Fault
SJF	San Jose Fault
SMFZ	Sierra Madre Fault Zone
WCF	Walnut Creek Fault
WF	Whittier Fault
SJFZ	San Jacinto Fault Zone
SAFZ	San Andreas Fault Zone

Bayesian array-based coherent RF method and multiple events at each station to constrain basin geometry by leveraging the close station-spacing of these short-term dense arrays to aid in suppressing the noise and non-uniqueness of the deconvolution process. The study showed promising lateral layers in the subsurface structure. Ghose et al. (2023) applied a traditional frequency domain deconvolution RF method to the nodal data set and showed complex, non-uniform basement topography, evidence of an intra-crustal interface, and a well-defined Moho discontinuity. Detailed information about the BASIN nodal deployment and RF work can be found in Clayton et al. (2019) and the respective studies mentioned above.

While these RFs studies imaged the sediment-basement interface, there are subtle lateral differences among the studies likely due to noise and rapid lateral variations in the structure. The use of gravity measurements along the lines helps distinguish the sediment-basement interface.

2.2. Residual Bouguer Gravity

We extracted Bouguer gravity station data for the northern basins from the Pan-America Center for Earth and Environmental Sciences gravity portal which included four independent gravity measurements (PACES, 2012; Figure S1 in Supporting Information S1). The gravity data obtained from PACES (2012) is no longer available but can be downloaded at http://dx.doi.org/10.22002/D1.20256. The Bouguer gravity points were interpolated to a 100-m spacing grid using a nearest-neighbor inverse-distance weighting interpolation scheme to create a Bouguer gravity map of the BASIN study area (Figure 2a).

We remove an estimated regional trend from the gravity values to highlight the basins' features. Because the estimation of the regional trend is subjective based on our interpretation of basin features, we used information gathered from the geologic map that highlights areas of exposed bedrock (Figure 1a), trends from the RF profiles, and borehole depths (Table S1 in Supporting Information S1). To determine the degree of polynomial detrending, we applied a least-squares method between the RFs time-to-basement and the gravity profiles reduced by polynomials with degrees between 1 and 7. We selected the polynomial degree with the lowest mean-squared error (Figure S2 in Supporting Information S1).

Figures 2b and 2c show the regional area included in the trend estimation for the San Gabriel basin and the Chino and San Bernardino basins, respectively. The regional trend of the San Gabriel basin was fitted using a second-order polynomial trend that included the San Gabriel Mountains to the north, Repetto Hills to the south, Montebello Hills to the southwest, and Eagle Rock Hills to the west while excluding the LAB (Figures 1a and 2b). Through our initial residual gravity calculation using a second order trend, it was clear the regional trend covering all three basins was not sufficient. The Chino and San Bernardino basins' residual gravity map was not much different from the Bouguer gravity map, suggesting that not enough long-wavelength features were removed. The San Gabriel basin map, however, showed most of the long-wavelength feature was removed and gave the clear structure of the basin. Thus, we separated the residual calculation for the San Gabriel basin from the Chino and San Bernardino basins. The San Bernardino and Chino showed the clearest basin structures with a seventh-order polynomial which covered the area of the San Jose Hills to the west, the eastern section of the San Gabriel Mountains to the north, the San Bernardino Mountains to the east, and the Jurupa Hills to the south (Figures 1a and 2c). The residual Bouguer gravity was obtained by subtracting the regional trend from the Bouguer gravity (Figures 2a and 2d).

Residual Bouguer gravity highlights the effect of subsurface density variations, including those due to the topography of the sediment-basement interface. There are different approaches to using residual Bouguer gravity to estimate crustal structure and the depth of sedimentary basins, especially when paired with another geophysical measurement. Tondi et al. (2019) employed a joint inversion of passive seismic and Bouguer gravity data to recover a 3D density model of Northern Italy. Florio (2020) used a depth-gravity relationship where known control points of basement rock depth are related to the residual Bouguer gravity to estimate the thickness of the Yucca flat basin, Nevada.

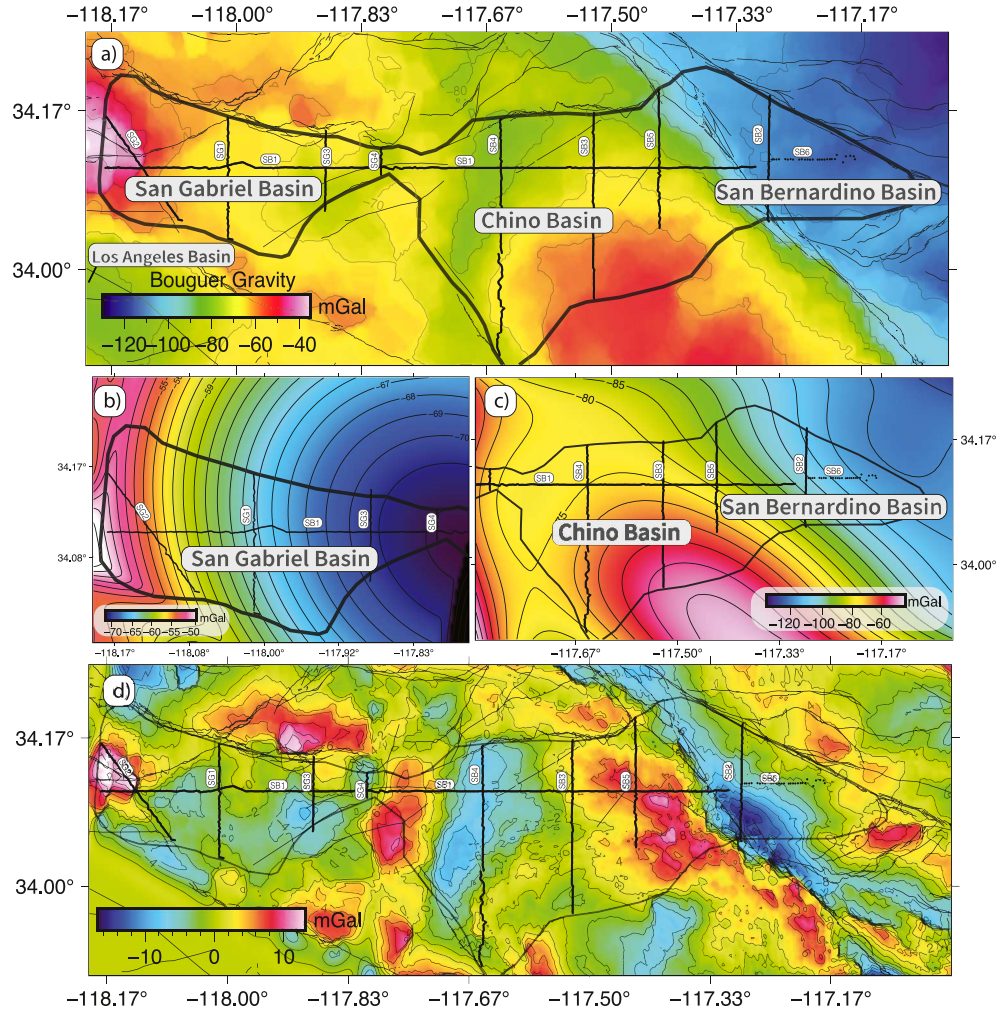

Figure 2. (a) Map of Bouguer gravity of the San Gabriel, Chino, and San Bernardino basins obtained from the PACES (2012) portal. (b) second order polynomial trend for San Gabriel basin. (c) seventh order polynomial trend for Chino and San Bernardino basins. (d) Residual Bouguer anomaly map. The black or gray outline shows the study area. Black points represent the 10 nodal BASIN lines.

2.3. Integration of Seismic and Gravity Measurements

We use Bouguer's formula for a basin embedded in a block of thickness H of density ρ_1, and a basin of thickness h with density ρ_2, given as

$$\delta g = 2\pi G(\rho_1)H + 2\pi G(\rho_2 - \rho_1)h \tag{1}$$

where G is the gravitational constant, to linearly relate the gravity anomaly to sedimentary layer density and thickness. This establishes a simple linear relationship between the residual Bouguer gravity, δg, and the travel time of the basement P-to-S converted phases, t,

$$\delta g = a + bt \tag{2}$$

where a and b are parameters determined by fitting δg and t. Expressing Equation 1 in the form of Equation 2 allows us to relate the residual gravity to the time-to-basement across the basins. Parameter a represents the Bouguer gravity of a block of thickness H with density ρ_1. Parameter b scales t so that it represents the contributions of a basin of thickness h and density ρ_2 relative to the embedded block. We solve for the parameters using Equation 2 with residual Bouguer gravity values and time-to-basement using a least-squares method for each of the 10 seismic lines. Since we have gravity values in a three-dimensional mesh, we interpolate the a

and b parameters from the lines to the three-dimensional mesh using an inverse-distance weighted interpolation scheme. We were then able to predict the time-to-basement away from the lines, constrained by the residual gravity anomaly values using the inverted Equation 2, $t = (\delta g - a)/b$. Thus, extending our two-dimensional study to a three-dimensional one.

2.4. Iterative Basement Depth Computation With Shear Wave Velocity Model

Depth to the basement was calculated using the predicted time obtained from Equation 2 and an *S*-wave velocity model. The formulas are a derivation of the standard travel time of the *P*-to-*S* converted phases from the RF (Zhu & Kanamori, 2000) assuming the ray parameter is zero:

$$t_{Ps} - t_P = \left(\frac{1}{\beta} - \frac{1}{\alpha}\right)h \tag{3}$$

$$t_{PpPs} - t_P = \left(\frac{1}{\beta} + \frac{1}{\alpha}\right)h \tag{4}$$

where h denotes the basin depth, β the *S*-wave velocity, α the *P*-wave velocity, t_P the direct *P*-arrival time, t_{Ps} the *Ps* arrival time, and t_{PpPs} the *PpPs* arrival time. We used Li et al. (2023) *S*-wave velocity model. We obtained *P*-wave velocities from *S*-wave velocities by using an empirical formula (Brocher, 2005) valid for *S*-wave velocities between 0 and 4.5 km/s excluding calcium-rich, mafic, gabbros, and serpentine rocks:

$$\alpha(\mathrm{km/s}) = 0.9409 + 2.0947\beta - 0.8206\beta^2 + 0.2683\beta^3 - 0.0251\beta^4 \tag{5}$$

Assuming the *P*-wave arrival is centered at 0 s and multiplying both sides of Equation 3 by $1/\beta$, we arrive at an initial depth equation.

$$h = \beta t_{Ps} \frac{K}{K-1} \tag{6}$$

where K is the V_p/V_s (α/β) ratio. Equation 6 was derived from Equation 3 and assumes a *Ps* phase recorded at sea level. We averaged the *S*-wave velocities across 1 km of the sedimentary column from the initial *S*-wave velocity model to compute K for each point in the mesh. Initial *P*-wave velocities were computed using Equation 5.

Li et al. (2023) then used the initial depth model as a prior for the *S*-wave velocity model inversion. The inversion of the V_s model is highly dependent on the initial model that uses the basin depth as a constraint. Using the *S*-wave velocity results, the depth was recalculated using Equation 3 or 4 depending on which converted phase is used. A linear relationship between the modeled depth and the predicted time-to-basement was established to fill in for the few points in the mesh that did not converge. We used an iterative process instead of solving an inverse problem because of the nonlinearity of the method. The prior basin model was provided for the V_s inversion and the new V_s model for the depth model calculations.

The algorithm outputs the estimated basement depth when the difference between *S*-wave travel time and *P*-wave travel time (3) or when the sum of *S* and *P*-wave travel time (4) approximately equaled the predicted time-to-basement. For the San Gabriel basin, we assumed a primary phase, *Ps*, while for the Chino and San Bernardino basins a *PpPs* phase. We proposed the *Ps* phase, labeled in the RF studies, for the Chino and San Bernardino instead is the *PpPs* phase. The justification behind this assumption was that the depth calculation did not converge to a value for times greater than ~1 s using the Ps phase and obtained unrealistic depths. On the other hand, the *PpPs* phase converged to values similar to previous literature and boreholes. For example, two boreholes in the Chino basin support a basin shallower than 2 km (Table S1 in Supporting Information S1). The Chino Basin Management program showed ~23 well boreholes penetrating crystalline bedrock to the west of SB4 and ~35 well boreholes penetrating sedimentary bedrock east of SB4 at shallow depths (<2 km; see Chino Basin Optimum Basin Management Program report (Wildermuth et al., 2005) for exact boreholes locations). In addition, multiple studies in the San Bernardino basin indicate measured depths of less than 2 km as mentioned in Section 1.1.

2.5. Integration of Borehole Basement Depths

Multiple borehole logs with recorded basement depths allowed us to constrain and corroborate our final depth model. There is a total of 17 borehole logs with recorded basement depths: 11 in the San Gabriel basin, 2 in

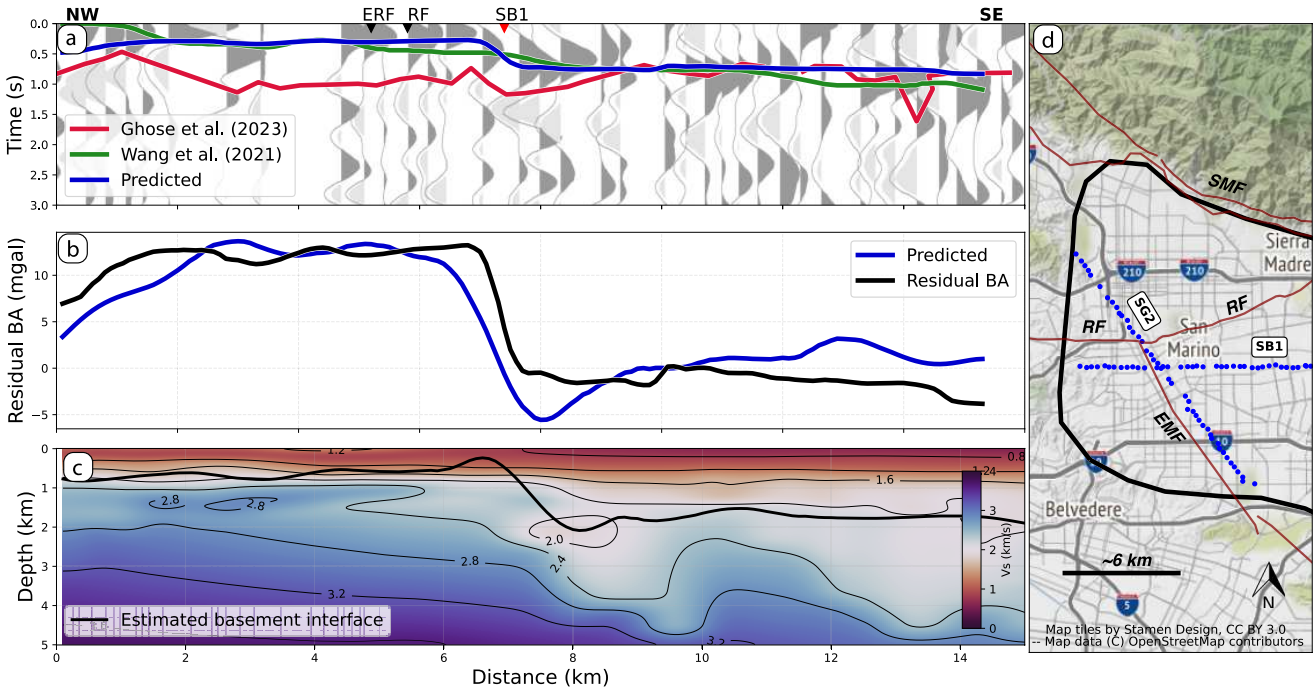

Figure 3. (a) Profile along SG2 showing the time-to-basement from two Receiver function (RF) studies and the predicted time-to-basement. RF background from Ghose et al. (2023). (b) Residual and predicted gravity anomaly. (c) *S*-wave velocity model and estimated depth. (d) Study area zoomed around the SG2 line. Fault names are found in Table 1.

the Chino basin, and 4 in the Raymond basin (Table S1 in Supporting Information S1). The boreholes in the San Gabriel basin were used to corroborate our model. Because the Chino basin contains only two borehole measurements, we assessed the model based on the closeness to the recorded depth and shifted all points in the Chino and SB basin mesh 500 m down to match the boreholes and previous maximum depths found in studies mentioned in Section 1.1. Borehole measurements provided another advantage in areas of poor interpolation of the inversion parameters. Such is the case in the Raymond basin where the interpolated parameters from Equation 2 are influenced by the gravity response and time-to-basement of SG2. It is difficult to evaluate this basin based on the response of SG2 because this line crosses the deeper SG basin and the edge of the Raymond basin. Thus, we followed a depth-gravity relation where the borehole depths were used as control points to estimate the basin depth. The four control borehole points (Table S1 in Supporting Information S1) are obtained from the Buwalda (1940) report.

3. Results

3.1. Profiles: Gravity and Time-To-Basement Linear Relationship

The residual Bouguer gravity map for the San Gabriel basin shows prominent gravity signatures over various geological features (Figure 1b). The highest gravity anomalies in the San Gabriel basin are shown in a triangular block near the intersection of SG2 and SB1. A steep gravity gradient extends from this intersection toward the Sierra Madre fault zone. The gravity profile along SG2 (Figure 3) reflects this gravity gradient anomaly (Figure 3b) in more detail than the RF profile (Figure 3a). Because of this, we modify the time-to-basement from the RFs to reflect this steep gravity gradient. Likewise, we adjusted the RF times along the SB1 line to reflect this gradient. Another gravity gradient trending northwest strikes subparallel to the East Montebello fault and the SG2 line. Furthermore, the north-central part of the San Gabriel basin shows higher gravity values than the south-central part. The predicted time-to-basement and gravity values of SG1 reflect this gravity trend (Figure 4). The misfit between the predicted time-to-basement to the RF time-to-basement from Wang et al. (2021) is similar through much of the line such that no modifications were required. The west-central and east-central sections of the basin have gravity lows, with the lowest values in the east-central part near line SG3 (Figure S3 in Supporting Information S1). Like SG1, line SG3 agreed with the RF results of Wang et al. (2021) interpretation. Gravity

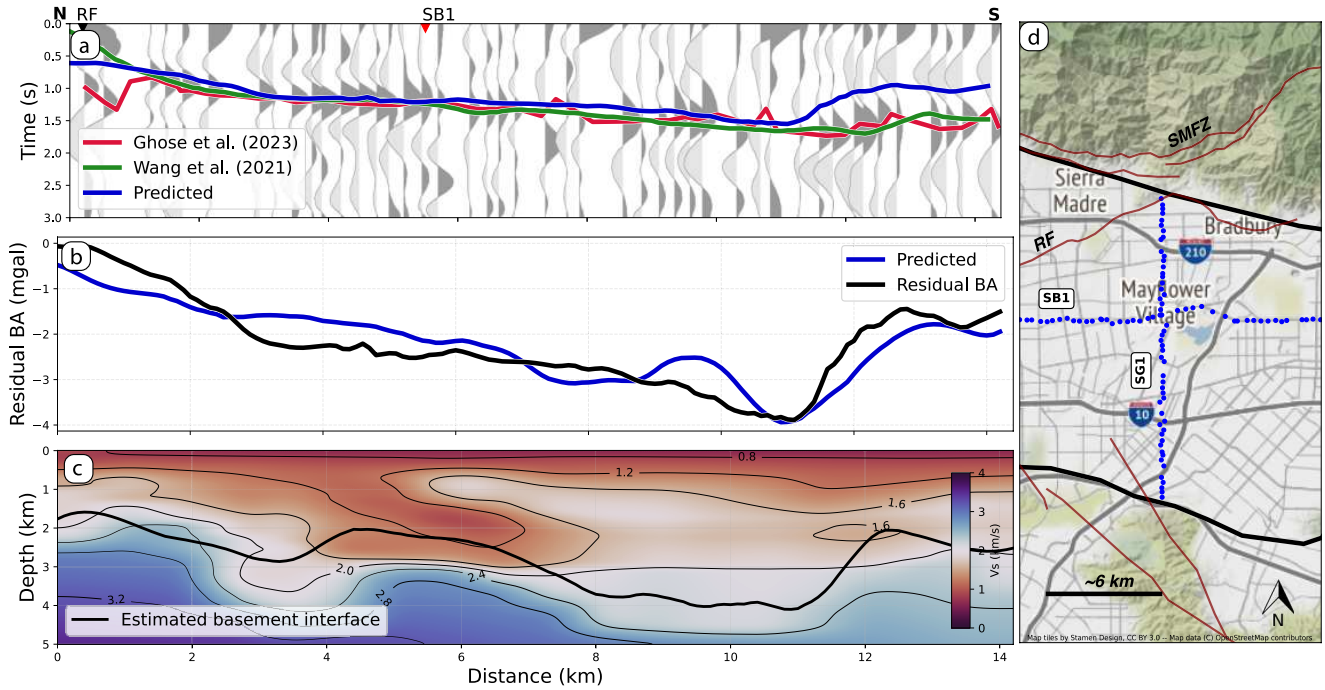

Figure 4. (a) Profile along SG1 showing the time-to-basement from two Receiver function (RF) studies and the predicted time-to-basement. RF background from Ghose et al. (2023). (b) Residual and predicted gravity anomaly. (c) *S*-wave velocity model and estimated depth. (d) Study area zoomed around the SG1 line. Fault names are found in Table 1.

lows around line SG4 (Figure S3 in Supporting Information S1) are enclosed with the east-central low of the San Gabriel basin.

The border between the San Gabriel and the Chino basins is best illustrated in the SG4 line since its located at both basins' extremities (Figure S3 in Supporting Information S1). This is an important area when determining the impact of the channeling waveguide effect. We needed to reinterpret the sediment basement interface in the RF profile because there was a large misfit between the predicted time-to-basement and the other studies' picks of the time-to-basement. The RF studies from Ghose et al. (2023) and Wang et al. (2021) show time-to-basement increasing to the south, with Wang et al. (2021) having slightly larger values in the south (Figure S3e in Supporting Information S1). The residual gravity signature, however, showed the gravity decreasing northwards, toward the base of the San Gabriel Mountains (Figure S3f in Supporting Information S1). It is quite possible that the residual gravity computation did not completely remove the edge effects or other possible short-wavelength features. To prevent the different polynomial trends from creating artifacts in the residual gravity map, we used the area around the SG4 line to ensure the residual Bouguer gravity values between both Chino and San Gabriel basins matched.

Separated approximately by line SB3, gravity highs are encountered in the east and lows in the west of the Chino basin (Figure 1b). All RF sediment-basement interfaces of the Chino basin were reinterpreted to a small extent using a combination of Ghose et al. (2023) and Wang et al. (2021). Line SB4 used Ghose et al. (2023)'s larger time-to-basement values in its northern section and Wang et al. (2021)'s smaller values in its southern section (Figure 5). Although the fit of the lines between the gravity anomalies and time-to-basement is not as good on a smaller scale, the general trend of gravity is maintained. Figure 5 shows the northern segment of line SB4 with the lowest gravity anomaly values. The center of the basin has a mix of low and high gravity anomalies. This trend continues to the SB3 profile which shows a longer travel time in its southern segment (Figure S4 in Supporting Information S1). The northern segment follows Wang et al. (2021) interpretation, favoring shorter travel times whereas the southern segment follows Ghose et al. (2023). The majority of the positive gravity anomalies are located southeast of the SB5 line except for a negative gradient anomaly to the north. Figure S5 in Supporting Information S1 shows the SB5 line gravity profile having the best fit with the northern shallow segment of Ghose et al. (2023). Whereas the southern segment of SB5 does not match well with either RF study, favoring a shorter travel time closer to Wang et al. (2021).

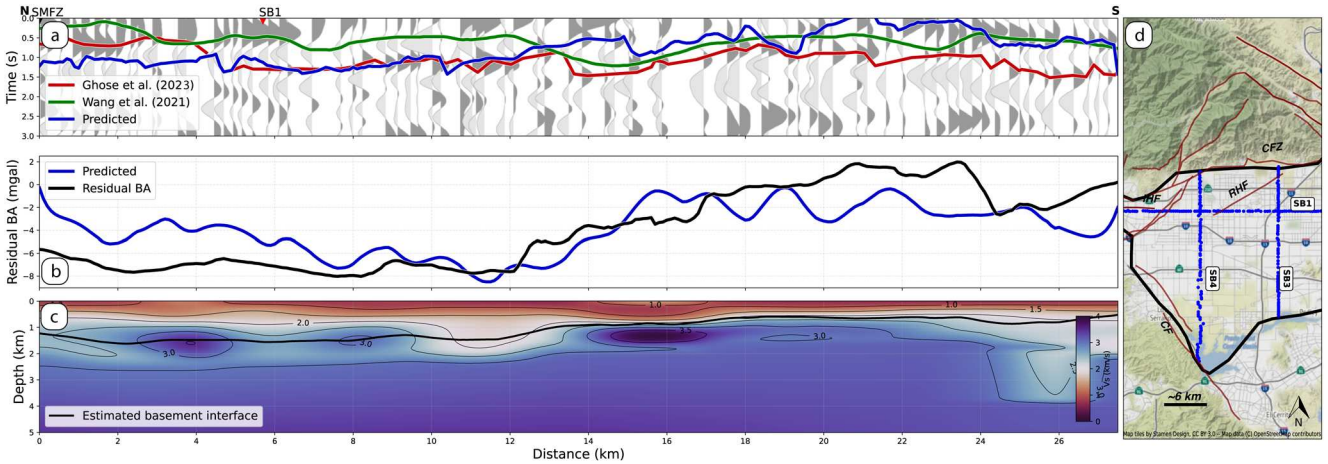

Figure 5. (a) Profile along SB4 showing the time-to-basement from two Receiver function (RF) studies and the predicted time-to-basement. RF background from Ghose et al. (2023). (b) Residual and predicted gravity anomaly. (c) *S*-wave velocity model and estimated depth. (d) Study area zoomed around the SB4 line. Fault names are found in Table 1.

Unlike the San Gabriel and Chino basins, the San Bernardino basin is mostly characterized by negative gravity anomalies (Figure 1b). A sharp gravity gradient follows the trace of the SJFZ, which also marks the boundary between the San Bernardino and Chino basins. The lowest gravity values are east of the southern segment of the SJFZ. The time-to-basement profile of SB2 captures a depocenter in this area which is also reflected in the gravity profile (Figure 6). The time-to-basement of line SB6 agrees with the gravity values getting more positive toward the root of the San Bernardino Mountains (Figure S6 in Supporting Information S1). Both lines have a good correlation between negative gravity values and longer time-to-basement along the SJFZ. The SB2 profile follows Wang et al. (2021) version of the sediment-basement interface and SB6 follows Ghose et al. (2023) values. It should be noted that Ghose et al. (2023) previous picks on SB2 did not agree with Wang et al. (2021)

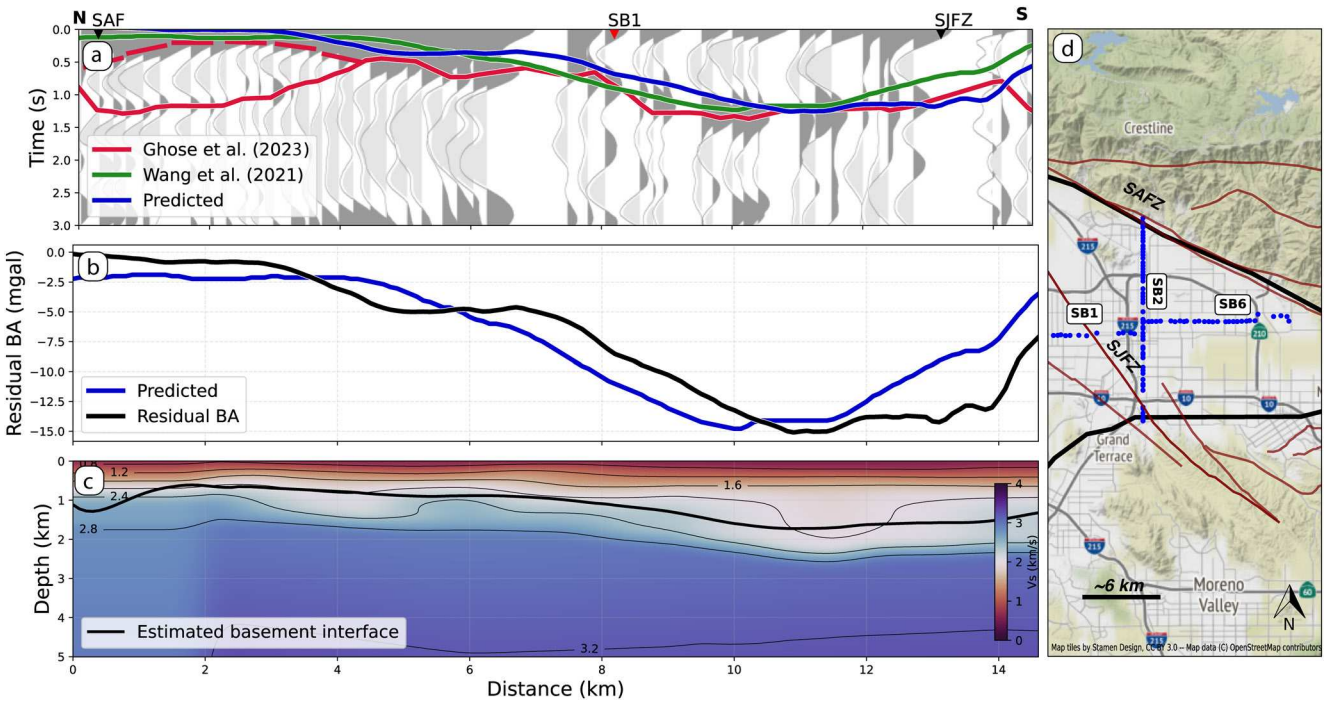

Figure 6. (a) Profile along SB2 showing the time-to-basement from two Receiver function (RF) studies and the predicted time-to-basement. RF background from Ghose et al. (2023). (b) Residual and predicted gravity anomaly. (c) *S*-wave velocity model and estimated depth. (d) Study area zoomed around the SB2 line. Fault names are found in Table 1.

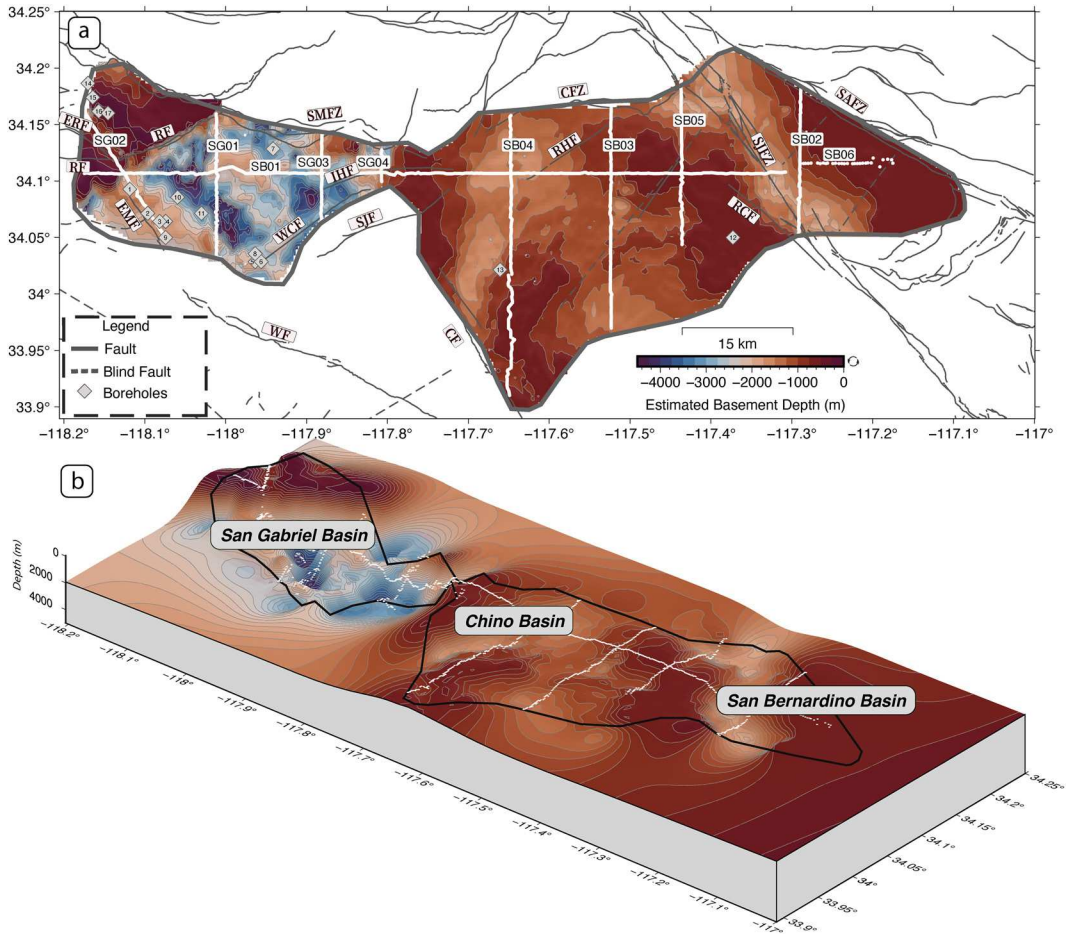

Figure 7. (a) Depth to basement map of the greater Los Angeles area's San Gabriel, Chino, and San Bernardino basins. The borehole numbers correspond to those listed in Table S1 in Supporting Information S1. (b) Three-dimensional perspective view from the southeast of basin depths. Basement depths are unconstrained outside the region shown in (a). The surface shows depth in meters below sea level. Small white circles represent the 10 nodal lines of the Basin Amplification Seismic Investigation survey. The thick dark gray line outlines the study area and encompasses the three basins. Solid black lines in (a) are faults and dashed black lines are blind faults. Fault names are shown in Table 1.

values for the northern section, but current picks do (dashed line). The southern section of SB2 shows the lowest gravity values in the basin and the time reflects this trend. The SB6 line also reflects this trend based on the lower negative values west of the line, which ends near the SB2 line.

3.2. 3D BASIN Depth Map

The depth model for the San Gabriel, Chino, and San Bernardino basins is shown in Figure 7. Although the basins share characteristics of subsidence, the geometries are unique. The San Gabriel basin's largest depressions of around 4.5 km are in the center and nonuniformly surrounded by shallow depths. Unlike the San Gabriel basin, the Chino basin has a simple geometry with the western side being deeper than the eastern side. On the western side, depths reach ∼1.5 km with the shallowest depths concentrated on the northern section and east-southern section of SB4 as well as the southern section of SB3 and northern section of SB5. The San Bernardino basin exhibits a much simpler geometry than the other basins with its major depression concentrated on the southwestern section of the basin with depths of ∼2 km. The basement depths increase gradually to 1 km toward the basin edge.

4. Discussion

The depth model shown in Figure 7 highlights geologic features such as faults, hills, and basins. The sensitivity of gravity to outline faults aided our interpretation of the San Gabriel basin's geometry. While Yeats (2004) called

the San Gabriel basin triangular-shaped, we distinguish it as parallelogram-shaped, bounded by the Raymond fault to the northwest, the Sierra Madre fault to the north, the San Jose fault to the east, and the East Montebello fault to the west. In the area between the western Raymond fault trace and the Eagle Rock fault, the positive gravity anomalies and the shallow depths reflect the displacement of old crystalline rocks of the San Rafael Hills from the Tertiary rocks (Buwalda, 1940). These might be a result of a restraining bend from the Raymond fault (Weaver & Dolan, 2000). Northeast of this area, the prominent gravity gradient delineates the eastern trace of the Raymond fault and is likely due to the offset of basement ridges, that juxtapose blocks with different basement elevations. This interpretation agrees with the Raymond fault acting as an impermeable barrier between the Raymond and San Gabriel basins (Buwalda, 1940).

The southeast gravity gradient and shallower depths delineate the East Montebello fault. The sedimentary layer thickness is not consistent along the strike of the fault. Basement depths are closer to 2–3 km in its southern segment (near boreholes 2, 3, 4, and 9) and 1 km to the north (near borehole 1) suggesting the fault may not be a purely right lateral fault. The fault may have a component of non-uniform vertical separation along the strike, allowing more accommodation space to be created at its southern end. This interpretation agrees with Yeats (2004) that the fault subsided more in its southwestern part than in the northeast. Hills are also highlighted by our model. For example, the Hacienda Hills just south of the San Gabriel basin have a positive gravity gradient and shallow basement depths nearby. While the Walnut Creek fault shows no tectonic geomorphic expression, it separates the flat-lying strata of the San Gabriel basin from folded strata of the San Jose and Puente Hills (Yeats, 2004). Figure S7 in Supporting Information S1 shows the modeled basin depth comparison to the borehole depths of the basement.

The structure of the Chino basin is broader and shallower than other basins. The deep segments close to SB4 are likely areas of sediment accumulation. In the southern segment of SB3, the increase in basement depths is likely due to the Jurupa Valley. South of SB5, the relatively shallow depths, and positive gravity anomalies reflect the exposed basement of the Jurupa Hills. We conclude that the Chino basin is deeper to the west than to the east. We corroborated the depth trends in our model with Wildermuth et al. (2005) which shows a series of boreholes penetrating crystalline bedrock in the east and sedimentary bedrock in the west at similar drilling depths (Figure S8 in Supporting Information S1). The shallower eastern side relative to the deeper western part of the Chino basin in the model reflects the shallower crystalline basement in the boreholes.

There is an interesting area of subsidence between the boundary of the Chino and San Bernardino basins not previously discussed in the literature. The residual gravity map shows anomalous gravity lows in contradiction to the general trend of positive values along the bases of mountains. We believe this is not an artifact created through the residual Bouguer calculations because we observe longer time-to-basement in the RFs of line SB5 which correlates well with the gravity trend. For example, Wang et al. (2021) obtained the largest time-to-basement values (close to 3 s) in this section which is a longer travel time than in the other profiles. This is anomalous because the San Gabriel basin is expected to have the deepest depths and the maximum time there is around 1.5 s. The times of Ghose et al. (2023) also show an agreement with the gravity but are more reasonable for the type of depths we expect in this basin (<2 km). Nevertheless, there is uncertainty in our geologic interpretation of this area. The gravity might be explained by the black belt of the magnetic mylonitic rocks of the southeastern San Gabriel Complex (Anderson et al., 2004; Nourse, 2002). The reason for the depth remains undetermined and is an area of further study.

The estimated basement shape of the San Bernardino basin suggests a pull-apart basin structure explained by extension along major strike-slip fault zones. There is ∼2 km subsidence associated with this strand of the SJFZ, which agrees well with other studies (Anderson et al., 2004, Figure S9 in Supporting Information S1). The low gravity values are associated with the basin fill comprised of unconsolidated Quaternary and Tertiary alluvial-fan deposits overlying the consolidated, non-water-bearing Tertiary deposits. The depths decrease steadily toward the western edge of the basin and are due to the metamorphic basement rock composition of the San Bernardino Mountains. Like other studies, we agree that the SAFZ has had little to no influence on the formation of the San Bernardino Basin. Most of the deformation and depocenters are along the SJFZ.

Although we assumed a simple linear relationship between Bouguer gravity and time-to-basement to calculate the basin depth, the depth model revealed unique sub-basin geometries that correspond well with previous studies and borehole datasets. However, we need to discuss the possible uncertainties in the inverted time-to-basement constrained by gravity and the depth map. Because the linear relationship assumes a constant density of the basin,

the misfits might be a cause of varying density rocks within the basin that are unaccounted for in Equation 3. Another source of the linear relationship uncertainty is the residual calculation error due to potentially not removing all longer wavelength gravity signatures in the Bouguer residual gravity calculation. While extensive work was done to remove the regional trend from the Bouguer gravity values, there might be areas where we could not capture all local effects pertaining to the basin. In Figure S10 in Supporting Information S1, we show an extreme method of evaluating the sensitivity of the lines to the modeled depth and time-to-basement inversion. The basin depth model is susceptible to systematic uncertainties present in the models used such as the V_s model and RFs, for which we point the reader to the respective studies for a detailed description.

5. Conclusion

The 3-D shape and depths of the northern LABs were computed by integrating seismic and Bouguer gravity measurements along with the surface and borehole geology. Due to the densely spaced constraints along 10 seismic lines, this approach was effective at determining the detailed geometry of the sediment-basement interface in an ∼90-km wide region extending from the southern SAFZ to the border of the LAB. Model validation against 17 borehole recorded basement depths allowed us to address non-uniqueness and trade-offs between seismic velocities and travel times. Gravity measurements constrained the 3-D shape of the sediment-basement interface and delineated the effects of faults around the basins. The basement shape and depths further contributed to improving a 3-D basin-scale V_s model (Li et al., 2023).

The parallelogram-shaped San Gabriel basin is a fault-bounded basin with a maximum depth of 4.5 km in its western and easternmost centers. The Chino basin is broader and substantially shallower than the San Gabriel basin and is dominated by a 1.5–2 km thick sedimentary layer in its western segment. The San Bernardino basin exhibits ∼2 km subsidence along the SJFZ, consistent with a pull-apart structure. Further work on ground motion simulations is needed to evaluate the seismic hazard and risk of the northern LABs and improve ground shaking models for large earthquake ruptures such as the forecasted M_w 7.8 on the southern San Andreas fault.

Data Availability Statement

The basement time was obtained from Liu et al. (2018), Wang et al. (2021), and Ghose et al. (2023). Li et al. (2023) provided the V_s model. The basement depths obtained from well borehole logs are publicly available through the Geologic Energy Management Division's (CalGEM) online mapping application Well Finder https://www.conservation.ca.gov/calgem/Pages/WellFinder.aspx, Chino Basin Optimum Basin Management Program (Wildermuth et al., 2005), and Buwalda (1940). The Bouguer gravity data was provided by the Pan American Center Earth and Environmental Science portal. Figures were plotted using the GMT software, PyGMT, and Cartopy (Met Office, 2010; Uieda et al., 2022; Wessel et al., 2019). The 3D basin depth model is publicly available at http://doi.org/10.22002/D1.20252.

Acknowledgments
We are grateful to the nodal deployment volunteers, Los Angeles residents, and business owners who hosted our instruments. We thank Liu et al. (2018), Wang et al. (2021), and Ghose et al. (2023) for providing their receiver function results, and Tom Brocher for sharing the borehole data. This research was supported by the National Science Foundation awards 2105358 and 2105320. The BASIN project was partly supported by U.S. Geological Survey awards GS17AP00002 and G19AP00015, and Southern California Earthquake Center awards 18029 and 19033. Data collection was supported by Louisiana State University and the California Institute of Technology. Nodal instruments were provided by Incorporated Research Institutions for Seismology (IRIS), Portable Array Seismic Studies of the Continental Lithosphere (PASSCAL), the University of Utah, Louisiana State University, and the University of Oklahoma.

References

Anderson, M., Matti, J., & Jachens, R. (2004). Structural model of the San Bernardino basin, California, from analysis of gravity, aeromagnetic, and seismicity data: Structure of the San Bernardino basin. *Journal of Geophysical Research*, *109*(B4), B04404. https://doi.org/10.1029/2003JB002544

Blomquist, W. (2021). The natural physical system of Chino Basin. In W. Blomquist (Ed.), *The realities of adaptive groundwater management* (Vol. 27, pp. 13–21). Springer International Publishing. https://doi.org/10.1007/978-3-030-63723-1_2

Brocher, T. M. (2005). Empirical relations between elastic wavespeeds and density in the earth's crust. *Bulletin of the Seismological Society of America*, *95*(6), 2081–2092. https://doi.org/10.1785/0120050077

Buwalda, J. P. (1940). *Geology of the Raymond basin* (pp. 1–131). California Institute of Technology. https://doi.org/10.22002/D1.20258

Catchings, R. D., Rymer, M. J., Goldman, M. R., Gandhok, G., & Steedman, C. E. (2008). *Structure of the San Bernardino basin along two seismic transects: Rialto-Colton fault to the San Andreas Fault and along the I-215 Freeway (I-10 to SR30) (report no. 2008–1197; version 1.0, open-file report)*. USGS Publications Warehouse. https://doi.org/10.3133/ofr20081197

Clayton, R., Persaud, P., Denolle, M., & Polet, J. (2019). Exposing Los Angeles's shaky geologic underbelly. In *Eos* (Vol. 100). https://doi.org/10.1029/2019EO135099

Denolle, M. A., Dunham, E. M., Prieto, G. A., & Beroza, G. C. (2014). Strong ground motion prediction using virtual earthquakes. *Science*, *343*(6169), 399–403. https://doi.org/10.1126/science.1245678

Dutcher, L. C., & Garrett, A. A. (1963). Geologic and hydrologic features of the San Bernardino area, California; with special reference to underflow across the San Jacinto fault. https://doi.org/10.3133/wsp1419

Florio, G. (2020). The estimation of depth to basement under sedimentary basins from gravity data: Review of approaches and the ITRESC method, with an application to the Yucca flat basin (Nevada). *Surveys in Geophysics*, *41*(5), 935–961. https://doi.org/10.1007/s10712-020-09601-9

Frankel, A. (1993). Three-dimensional simulations of ground motions in the San Bernardino Valley, California, for hypothetical earthquakes on the San Andreas fault. *Bulletin of the Seismological Society of America*, *83*(4), 1020–1041. https://doi.org/10.1785/BSSA0830041020

Fuis, G. S., Ryberg, T., Godfrey, N. J., Okaya, D. A., & Murphy, J. M. (2001). Crustal structure and tectonics from the Los Angeles basin to the Mojave desert, southern California. *Geology*, *29*(1), 15–18. https://doi.org/10.1130/0091-7613(2001)029<0015:CSATFT>2.0.CO;2

Ghose, R., Persaud, P., & Clayton, R. W. (2023). Basin structure for earthquake ground motion estimates in Urban Los Angeles mapped with nodal receiver functions. https://doi.org/10.22541/essoar.167591060.08077421/v1

Jennings, C. W., & Bryant, W. A. (2010). *Fault activity map of California (version 2.0) [map]*. Department of Conservation, California Geological Survey. Retrieved from https://maps.conservation.ca.gov/cgs/metadata/GDM_006_FAM_750k_v2_metadata.html

Li, Y., Villa, V., Clayton, R., & Persaud, P. (2023). Shear wave velocities in the San Gabriel and San Bernardino basins, California. https://doi.org/10.1002/essoar.10512118.1

Liu, G., Persaud, P., & Clayton, R. W. (2018). Structure of the northern Los Angeles basins revealed in teleseismic receiver functions from short-term nodal seismic arrays. *Seismological Research Letters*, *89*(5), 1680–1689. https://doi.org/10.1785/0220180071

Magistrale, H., Day, S. M., Clayton, R. W., & Graves, R. (2000). The SCEC southern California reference three-dimensional seismic velocity model version 2. *Bulletin of the Seismological Society of America*, *90*(6B), S65–S76. https://doi.org/10.1785/0120000510

Met Office. (2010). Cartopy: A cartographic python library with a Matplotlib interface. Retrieved from http://scitools.org.uk/cartopy

Morton, D. M., & Miller, F. K. (2006). Geologic map of the San Bernardino and Santa Ana 30' × 60' quadrangles, California [map]. Retrieved from https://pubs.usgs.gov/of/2006/1217/

Nourse, J. A. (2002). Middle Miocene reconstruction of the central and eastern San Gabriel mountains, southern California, with implications for evolution of the San Gabriel fault and Los Angeles basin. In A. Barth (Ed.), *Contributions to crustal evolution of the southwestern United States*. Geological Society of America. https://doi.org/10.1130/0-8137-2365-5.161

Olsen, K. B., Day, S. M., Minster, J. B., Cui, Y., Chourasia, A., Faerman, M., et al. (2006). Strong shaking in Los Angeles expected from southern San Andreas earthquake. *Geophysical Research Letters*, *33*(7), L07305. https://doi.org/10.1029/2005GL025472

PACES. (2012). Pan-American Center for Earth and Environmental Studies. Retrieved from http://gis.utep.edu/paces/PACES%20Gravity%20Magnetics.htm

Stephenson, W. J. (2002). Delineation of faulting and basin geometry along a seismic reflection transect in urbanized san Bernardino valley, California. *Bulletin of the Seismological Society of America*, *92*(6), 2504–2520. https://doi.org/10.1785/0120010222

Tondi, R., Vuan, A., Borghi, A., & Argnani, A. (2019). Integrated crustal model beneath the Po Plain (Northern Italy) from surface wave tomography and Bouguer gravity data. *Tectonophysics*, *750*, 262–279. https://doi.org/10.1016/j.tecto.2018.10.018

Uieda, L., Tian, D., Leong, W. J., Jones, M., Schlitzer, W., Grund, M., et al. (2022). PyGMT: A Python interface for the generic mapping tools (v0.7.0). *Zenodo*. https://doi.org/10.5281/zenodo.6702566

Wang, X., Zhan, Z., Zhong, M., Persaud, P., & Clayton, R. W. (2021). Urban Basin structure imaging based on dense arrays and Bayesian array-based coherent receiver functions. *Journal of Geophysical Research: Solid Earth*, *126*(9). https://doi.org/10.1029/2021JB022279

Weaver, K. D., & Dolan, J. F. (2000). Paleoseismology and geomorphology of the Raymond fault, Los Angeles county, California. *Bulletin of the Seismological Society of America*, *90*(6), 1409–1429. https://doi.org/10.1785/0119990075

Wessel, P., Luis, J. F., Uieda, L., Scharroo, R., Wobbe, F., Smith, W. H. F., & Tian, D. (2019). The generic mapping tools version 6. *Geochemistry, Geophysics, Geosystems*, *20*(11), 5556–5564. https://doi.org/10.1029/2019GC008515

Wildermuth, M. J., LeClaire, J. P., Malone, A. E., Hwang, J. H., Rossi, J. V., & Atwater, R. (2005). Chino Basin optimum basin management program. In *Managing watersheds for human and natural impacts* (pp. 1–12). American Society of Civil Engineers. https://doi.org/10.1061/40763(178)140

Wright, T. L. (1991). Chapter 3 Structural geology and tectonic evolution of the Los Angeles basin, California. https://doi.org/10.1306/M52531C3

Yeats, R. S. (2004). Tectonics of the San Gabriel basin and surroundings, southern California. *Geological Society of America Bulletin*, *116*(9), 1158. https://doi.org/10.1130/B25346.1

Yerkes, R. F., & Campbell, R. H. (2005). *Preliminary geologic map of the Los Angeles 30' × 60' Quadrangle, Southern California [map]*. U.S. Geological Survey. Retrieved from https://pubs.usgs.gov/of/2005/1019/

Zhu, L., & Kanamori, H. (2000). Moho depth variation in southern California from teleseismic receiver functions. *Journal of Geophysical Research*, *105*(B2), 2969–2980. https://doi.org/10.1029/1999JB900322